

Journal of Fluid Mechanics

<http://journals.cambridge.org/FLM>

Additional services for *Journal of Fluid Mechanics*:

Email alerts: [Click here](#)

Subscriptions: [Click here](#)

Commercial reprints: [Click here](#)

Terms of use : [Click here](#)



Dynamics of steep two-dimensional gravity–capillary solitary waves

PAUL A. MILEWSKI, J.-M. VANDEN-BROECK and ZHAN WANG

Journal of Fluid Mechanics / Volume 664 / December 2010, pp 466 - 477

DOI: 10.1017/S0022112010004714, Published online: 01 November 2010

Link to this article: http://journals.cambridge.org/abstract_S0022112010004714

How to cite this article:

PAUL A. MILEWSKI, J.-M. VANDEN-BROECK and ZHAN WANG (2010). Dynamics of steep two-dimensional gravity–capillary solitary waves. *Journal of Fluid Mechanics*, 664, pp 466–477
doi:10.1017/S0022112010004714

Request Permissions : [Click here](#)

Dynamics of steep two-dimensional gravity–capillary solitary waves

PAUL A. MILEWSKI¹†, J.-M. VANDEN-BROECK²
AND ZHAN WANG¹

¹Department of Mathematics, University of Wisconsin-Madison, Madison, WI 53706, USA

²Department of Mathematics, University College London, London WC1E 6BT, UK

(Received 28 May 2010; revised 3 September 2010; accepted 8 September 2010;
first published online 1 November 2010)

In this paper, the unsteady evolution of two-dimensional fully nonlinear free-surface gravity–capillary solitary waves is computed numerically in infinite depth. Gravity–capillary wavepacket-type solitary waves were found previously for the full Euler equations, bifurcating from the minimum of the linear dispersion relation. Small and moderate amplitude elevation solitary waves, which were known to be linearly unstable, are shown to evolve into stable depression solitary waves, together with a radiated wave field. Depression waves and certain large amplitude elevation waves were found to be robust to numerical perturbations. Two kinds of collisions are computed: head-on collisions whereby the waves are almost unchanged, and overtaking collisions which are either almost elastic if the wave amplitudes are both large or destroy the smaller wave in the case of a small amplitude wave overtaking a large one.

Key words: capillary waves, solitary waves, surface gravity waves

1. Introduction

In this paper, two-dimensional gravity–capillary solitary waves travelling on the surface of a fluid of infinite depth with a velocity $c < c_{min}$ are considered. Here c_{min} is the minimum phase velocity of linear waves

$$c_{min} = \left(\frac{4g\sigma}{\rho} \right)^{1/4}, \quad (1.1)$$

where σ is the constant coefficient of surface tension, g is the acceleration due to gravity and ρ is the fluid density. Longuet-Higgins (1989), Vanden-Broeck & Dias (1992) and Dias, Menasce & Vanden-Broeck (1996) first computed branches of solitary waves which have either a positive free-surface elevation at their centre – denoted waves of elevation – or a negative free-surface elevation at their centre – denoted waves of depression. Iooss & Kirrmann (1996) proved the existence of these two branches for $c_{min} - c > 0$ small. Analytical approximations for these branches of solitary waves were given by Dias & Iooss (1993). At small amplitude, the envelope of these waves can be approximated by the focusing nonlinear Schrödinger (NLS) equation's solitary wave solution from which the wavepacket solitary travelling wave is

† Email address for correspondence: milewski@math.wisc.edu

obtained since the phase and group speed are equal at the minimum of the dispersion relation. More recently, fully localized three-dimensional solitary waves (lumps) were found in this regime by Parau, Vanden-Broeck & Cooker (2005).

There are relatively fewer studies on the stability and dynamics of gravity–capillary solitary waves. In the shallow water limit and for the Bond number less than or near $1/3$, there are dynamical simulations based on model equations such as the fifth-order Korteweg–de Vries (KdV) equation in two dimensions or the Kadomtsev–Petviashvili (KP) or Benney–Luke equation in three dimensions. These regimes imply a very thin fluid layer of less than 0.5 cm for water. Of note is the work of Malomed & Vanden-Broeck (1996) who study solitary wave interactions within the fifth-order KdV equation, Berger & Milewski (2000) who study the generation of fully localized three-dimensional waves by a pressure forcing in a model Benney–Luke equation, and Grimshaw, Maleewong & Asanavant (2009) who study the stability of Euler free-surface flows with a pressure forcing in the shallow limit.

In the deep water limit, which, due to the wavelength of these waves requires only a few centimetres of water, Calvo, Yang & Akylas (2002) computed the spectral stability of waves along the two branches. They found that the depression branch was stable and the elevation branch unstable at small and moderate amplitudes, becoming stable at a point far along the branch, where the elevation wave resembles two depression waves placed side-by-side. Recent theoretical work has proved existence and a type of stability for waves in this regime (see Groves & Wahlén 2010 and references therein). The stability of two-dimensional waves to three-dimensional perturbations has been studied in shallow water (Bond number less than $1/3$) by Kadomtsev & Petviashvili (1970), whereas in deep water, variational arguments have been applied to the gravity–capillary case by Kim & Akylas (2007). In both cases transverse instabilities are predicted, and these are related to the eventual existence of lumps. Computations of the dynamics of solitary waves have been restricted to model equations by Akers & Milewski (2008) (for two-dimensional fluids) and Akers & Milewski (2010) for three dimensions. To our knowledge there have been no computations of the dynamics of gravity–capillary solitary waves, using the full Euler equations.

On the experimental side, Zhang (1995) performed early experiments on three-dimensional gravity–capillary waves in a wind-wave tank and observed isolated steep surface dips believed to be localized lumps. More recently, Falcon, Laroche & Fauve (2002) have carried out careful experiments to observe depression solitary waves in very shallow layer of mercury, and Diorio *et al.* (2009) have generated fully localized three-dimensional wavepacket solitary waves in deep water and simulated the results with the model equation developed by Akers & Milewski (2009).

The formulation of the problem is considered in §2 and the numerical results are presented in §3.

2. Formulation

Consider a two-dimensional, irrotational free-surface flow of an inviscid, incompressible fluid of infinite depth in the presence of gravity and capillary forces. The governing equations for the flow are

$$\Delta\bar{\phi} = 0 \quad \text{for } -\infty < y < \bar{\zeta}(x, t), \quad (2.1)$$

$$\bar{\phi} \rightarrow 0 \quad \text{as } y \rightarrow -\infty, \quad (2.2)$$

$$\bar{\zeta}_t + \bar{\phi}_x \bar{\zeta}_x = \bar{\phi}_y \quad \text{at } y = \bar{\zeta}(x, t), \tag{2.3}$$

$$\bar{\phi}_t = -\frac{1}{2} [\bar{\phi}_x^2 + \bar{\phi}_y^2] - \bar{\zeta} + \frac{\bar{\zeta}_{xx}}{(1 + \bar{\zeta}_x^2)^{3/2}} \quad \text{at } y = \bar{\zeta}(x, t). \tag{2.4}$$

The equations were made dimensionless by choosing $(\sigma/\rho g)^{1/2}$ and $(\sigma/\rho g^3)^{1/4}$ as the units of length and time. The free surface is denoted by $y = \bar{\zeta}(x, t)$ and $\bar{\phi}$ is the velocity potential. Equations (2.3) and (2.4) are the kinematic and dynamic boundary conditions at the free surface.

The main idea to handle the unknown free surface computationally is to reformulate this system, based on a time-dependent conformal map from the physical domain to the lower half-plane with horizontal and vertical coordinates denoted by ξ and η , respectively. Such a method was pioneered by Dyachenko, Zakharov & Kuznetsov (1996) and used, for example, by Li, Hyman & Choi (2004). The map can be found by solving the harmonic boundary value problem

$$y_{\xi\xi} + y_{\eta\eta} = 0 \quad \text{for } -\infty < \eta < 0, \tag{2.5}$$

$$y = Y(\xi, t) \quad \text{at } \eta = 0, \tag{2.6}$$

$$y \sim \eta \quad \text{as } \eta \rightarrow -\infty, \tag{2.7}$$

where $Y(\xi, t) = \bar{\zeta}(x(\xi, 0, t), t)$. The harmonic conjugate variable $x(\xi, \eta, t)$ is defined through the Cauchy–Riemann relations for the complex function $z(\xi, \eta, t) = x(\xi, \eta, t) + iy(\xi, \eta, t)$. In the transformed plane, the velocity potential $\phi(\xi, \eta, t) \triangleq \bar{\phi}(x(\xi, \eta, t), y(\xi, \eta, t), t)$ and its harmonic conjugate $\psi(\xi, \eta, t)$ also satisfy Laplace’s equation. Thus,

$$\phi_{\xi\xi} + \phi_{\eta\eta} = 0 \quad \text{for } -\infty < \eta < 0, \tag{2.8}$$

$$\phi = \Phi(\xi, t) \quad \text{at } \eta = 0, \tag{2.9}$$

$$\phi \rightarrow 0 \quad \text{as } \eta \rightarrow -\infty, \tag{2.10}$$

where $\Phi(\xi, t) \triangleq \phi(\xi, 0, t)$. Defining $\Psi(\xi, t) \triangleq \psi(\xi, 0, t)$ and $X(\xi, t) \triangleq x(\xi, 0, t)$, from elementary harmonic analysis we have that

$$\Psi = \mathcal{H}[\Phi], \quad X = \xi - \mathcal{H}[Y], \tag{2.11}$$

where \mathcal{H} is the Hilbert transform

$$\mathcal{H}[f] = \int_{-\infty}^{\infty} \frac{f(\xi', 0, t)}{\xi' - \xi} d\xi'. \tag{2.12}$$

Next, we shall write the evolution equations for Y and Φ using the boundary conditions at the free surface. By application of the chain rule, since $Y(\xi, t) = \bar{\zeta}(x(\xi, 0, t), t)$, $\Phi(\xi, t) = \bar{\phi}(x(\xi, 0, t), y(\xi, 0, t), t)$ and $\Psi(\xi, t) = \bar{\psi}(x(\xi, 0, t), y(\xi, 0, t), t)$, we have

$$Y_t = \bar{\zeta}_x X_t + \bar{\zeta}_t, \tag{2.13}$$

$$Y_\xi = \bar{\zeta}_x X_\xi, \tag{2.14}$$

$$\Phi_t = \bar{\phi}_t + \bar{\phi}_x X_t + \bar{\phi}_y Y_t, \tag{2.15}$$

$$\Phi_\xi = \bar{\phi}_x X_\xi + \bar{\phi}_y Y_\xi, \tag{2.16}$$

$$\Psi_\xi = \bar{\psi}_x X_\xi + \bar{\psi}_y Y_\xi = -\bar{\phi}_y X_\xi + \bar{\phi}_x Y_\xi. \tag{2.17}$$

Using these formulas, the kinematic and dynamics boundary conditions (2.3) and (2.4) now read

$$\Psi_\xi = X_t Y_\xi - Y_t X_{\xi\xi}, \tag{2.18}$$

$$\Phi_t = -\frac{1}{2} \frac{\Phi_\xi^2 + \Psi_\xi^2}{J} - Y + \frac{X_\xi Y_{\xi\xi} - Y_\xi X_{\xi\xi\xi}}{J^{3/2}} + \frac{X_t X_\xi + Y_t Y_\xi}{J} \Phi_\xi + \frac{X_t Y_\xi - Y_t X_\xi}{J} \Psi_\xi, \tag{2.19}$$

where $J = X_\xi^2 + Y_\xi^2$. Furthermore, X_t and Y_t are not independent. Notice that z_t/z_ξ is an analytic function of $\xi + i\eta$, and that it, therefore, follows that the real and imaginary part of their boundary values are related also by the Hilbert transform:

$$\text{Im}\left(\frac{z_t}{z_\xi}\right)_{\eta=0} = \frac{Y_t X_\xi - X_t Y_\xi}{J} = -\frac{\Psi_\xi}{J}, \quad \text{Re}\left(\frac{z_t}{z_\xi}\right)_{\eta=0} = \frac{Y_t Y_\xi + X_t X_\xi}{J} = \mathcal{H}\left[\frac{\Psi_\xi}{J}\right]. \tag{2.20}$$

Solving for X_t and Y_t ,

$$X_t = X_\xi \mathcal{H}\left[\frac{\Psi_\xi}{J}\right] + Y_\xi \left(\frac{\Psi_\xi}{J}\right), \tag{2.21}$$

$$Y_t = Y_\xi \mathcal{H}\left[\frac{\Psi_\xi}{J}\right] - X_\xi \left(\frac{\Psi_\xi}{J}\right). \tag{2.22}$$

Inserting these relations into (2.18) and (2.19) together with (2.11), we obtain the surface Euler system

$$X_\xi = 1 - \mathcal{H}[Y_\xi], \tag{2.23}$$

$$\Psi_\xi = \mathcal{H}[\Phi_\xi], \tag{2.24}$$

$$Y_t = Y_\xi \mathcal{H}\left[\frac{\Psi_\xi}{J}\right] - X_\xi \left(\frac{\Psi_\xi}{J}\right), \tag{2.25}$$

$$\Phi_t = \frac{1}{2} \frac{\Psi_\xi^2 - \Phi_\xi^2}{J} - Y + \frac{X_\xi Y_{\xi\xi} - Y_\xi X_{\xi\xi\xi}}{J^{3/2}} + \Phi_\xi \mathcal{H}\left[\frac{\Psi_\xi}{J}\right]. \tag{2.26}$$

Given initial values for Φ and Y , X_ξ and Ψ_ξ can be calculated with the first two equations, and Φ and Y can then be advanced in time with the last two equations.

The numerical integration of the surface Euler system is accomplished with a Fourier spectral discretization of the ξ dependence, where all derivatives and Hilbert transforms are computed spectrally. We use that the Fourier symbol of \mathcal{H} is $i\text{sgn}(k)$, that is, if

$$\hat{q}(k) = \mathcal{F}[q(\xi)] = \int_{-\infty}^{\infty} q(\xi) e^{-ik\xi} d\xi, \tag{2.27}$$

then,

$$\mathcal{H}[q] = \mathcal{F}^{-1}[i\text{sgn}(k)\mathcal{F}[q]]. \tag{2.28}$$

Nonlinear terms are computed in real space and dealiased, and a fourth-order Runge–Kutta method is used to advance the solution in time. The surface Euler system has, of course, the same conserved quantities as the original Euler equations (2.1)–(2.4), which we will use to monitor the errors in the computations. The mass, M , horizontal momentum, P , and energy, E , are given by

$$M = \int Y X_\xi d\xi, \quad P = \int Y \Phi_\xi d\xi, \quad E = \frac{1}{2} \int \Psi \Phi_\xi d\xi + \int (\sqrt{J} - X_\xi) d\xi + \frac{1}{2} \int Y^2 X_\xi d\xi. \tag{2.29}$$

These quantities are conserved up to a relative error of less than 10^{-8} throughout our computations. Such accuracy was necessary to detect, in certain cases, small ‘inelasticities’ in certain collisions. A more detailed view of the error is shown in figure 6.

The classical dispersion relation can be recovered from the linearized equations which are obtained by taking Y , Φ_ξ and Ψ_ξ small and $X_\xi \sim 1$ and $J \sim 1$

$$Y_t = -\mathcal{H}[\Phi_\xi], \quad (2.30)$$

$$\Phi_t = -Y + Y_{\xi\xi}, \quad (2.31)$$

which yields the dispersion relation

$$\omega^2 = |k|(1 + k^2). \quad (2.32)$$

In our scaled variables, the phase speed c has a minimum of $\sqrt{2}$ at $k = 1$ from which the solitary waves will bifurcate.

3. Results

3.1. Travelling waves

Seeking travelling solutions to the Euler equations (2.1)–(2.4) with wave speed, c , we assume all functions to depend on $x - ct$ and replace (2.3), (2.4) with

$$-c\bar{\zeta}_x = -\bar{\phi}_x\bar{\zeta}_x + \bar{\phi}_y \quad (3.1)$$

$$-c\bar{\phi}_x = -\frac{1}{2} [\bar{\phi}_x^2 + \bar{\phi}_y^2] - \bar{\zeta} + \frac{\bar{\zeta}_{xx}}{(1 + \bar{\zeta}_x^2)^{3/2}}. \quad (3.2)$$

A similar calculation to that of the previous section results in $\Psi = cY$ and the dynamic boundary condition (2.26) is replaced by

$$\frac{c^2}{2} \left(\frac{1}{J} - 1 \right) + Y + \frac{Y_\xi X_{\xi\xi} - X_\xi Y_{\xi\xi}}{J^{3/2}} = 0. \quad (3.3)$$

This, together with $X_\xi = 1 - \mathcal{H}[Y_\xi]$, completes an integro-differential system for finding Y . From this Φ is found by using $\Phi = -c\mathcal{H}[Y]$, completing the initial data needed for the surface Euler system. These equations for travelling waves are equivalent to the system solved by Vanden-Broeck & Dias (1992) under a different scaling.

Numerically, the equations are discretized spectrally with Fourier modes in ξ and solved for the Fourier coefficients by Newton’s method. In most calculations, 2048 or 4096 modes were used so as to give appropriately resolved initial data for the time-dependent computations. The elevation and depression branches of waves discussed in §1, together with typical profiles, are shown in figure 1. One can note that the small amplitude asymptotics (based on an NLS equation) is only applicable at very small amplitudes which had been noted earlier by Dias & Iooss (1993) and Akers & Milewski (2009). Furthermore, the NLS equation does not predict any of the dynamical phenomena observed. It is also instructive to show the bifurcation curves using the energy instead of the centre free-surface displacement as the amplitude parameter (see figure 2a). In this figure, the elevation and depression branches are almost equal up to $E \approx 0.3$, where they change behaviour abruptly with the elevation branch having a less rapid increase in energy than the depression one. At large amplitudes, one can see that the elevation wave has approximately twice the energy of the depression wave, matching the intuition that these waves are similar to two depression waves placed side-by-side.

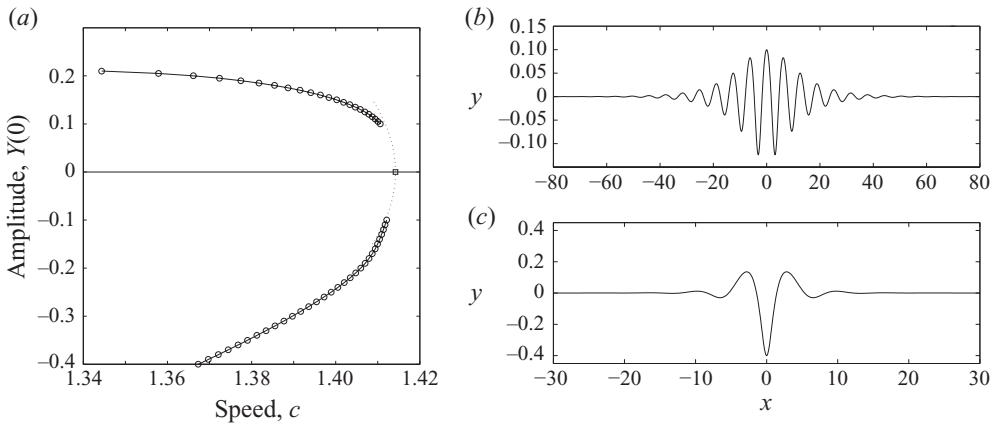


FIGURE 1. (a) Elevation and depression branches of the solution together with the bifurcation point at $c = \sqrt{2}$ and the small amplitude asymptotic prediction (dashed curve). Typical free-surface profiles: an elevation wave (b) at the right endpoint of the computed elevation branch ($Y(0) = 0.1$ and $c = 1.4106$) and a depression wave (c) at the left endpoint of the computed depression branch ($Y(0) = -0.4$ and $c = 1.3660$). Note that the vertical scale is greatly magnified relative to the horizontal scale and that the smaller amplitude depression wavepacket has a carrier wavelength of approximately 2π corresponding to $k = 1$.

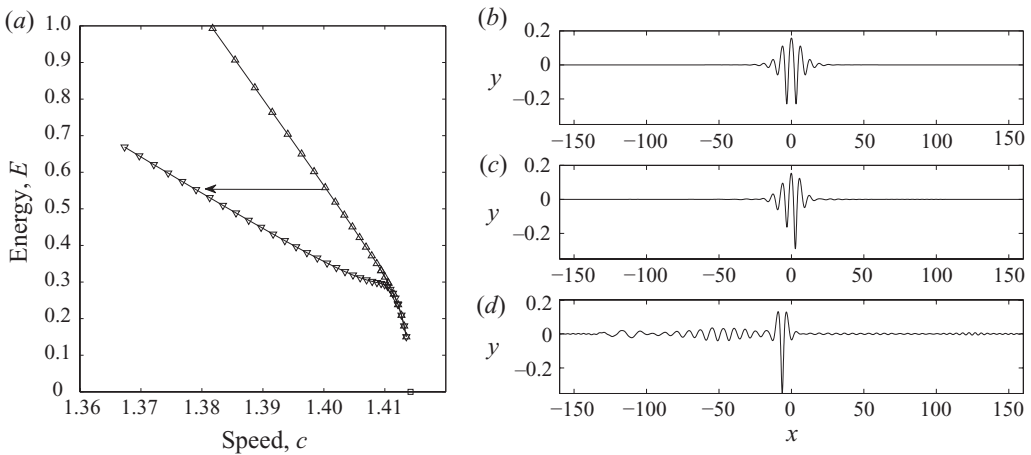


FIGURE 2. (a) The elevation and depression branches (up and down triangles, respectively) are parameterized by the energy of the solution. (b–d) Three free-surface profiles are shown for the instability of an elevation wave: $t = 0$ (b), $t = 150$ (c) and $t = 600$ (d). The profiles are shown in a frame of reference moving to the right with the speed of the initial elevation wave ($c = 1.4002$). Its initial amplitude is $Y(0) = 0.15$. The arrow in (a) indicates the transition between the initial and final solitary waves of the time evolution.

3.2. Dynamics

3.2.1. Instability

The first dynamical computational experiment presented is the evolution of an unstable elevation wave and is shown in figure 2. Various perturbations to the depression wave were tried (with magnitudes up to 10 % of the initial wave) yielding

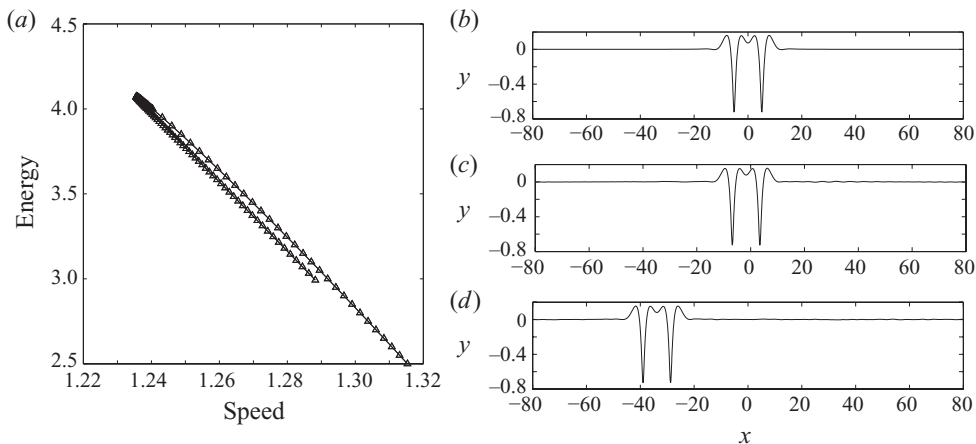


FIGURE 3. (a) A portion of the large amplitude elevation branch is shown, with a turning point at $E \approx 4.0673$ and $c \approx 1.2357$. Along the lower part of the branch the waves are stable according to our computations. (b–d) Three free-surface profiles are shown in the dynamics of a perturbed (5% perturbation) elevation wave: $t = 0$ (b), $t = 125$ (c) and $t = 2500$ (d). The profiles are shown in a frame of reference moving to the right with the speed of the initial elevation wave ($c = 1.2882$). Its initial energy is $E = 2.9926$ corresponding to the last point shown on the branch (the branch continues but was not computed beyond this point).

always similar results: the instability manifests itself by a growing asymmetry in the central troughs, where the leading trough grows to become the single central trough of the larger amplitude and slower depression wave. There is a radiated wave field of linear wave packets shed on both sides of the solitary wave. The waves shed behind the solitary waves are longer, with $k > 1$ so that their group speed permits the energy to travel at speeds below that of the solitary wave. Shorter waves are shed ahead of the solitary wave. Given that the computations are performed in a periodic domain, the evolution is shown only until the radiated waves have wrapped around the domain. We note, however, that the computations were continued to much longer times and that the remaining depression solitary wave is robust and persists in a sea of small amplitude gravity–capillary waves. One can estimate the amplitude of the resulting depression wave by observing that very little energy is radiated away during the dynamics: in the example shown only approximately 1% of the energy of the original solitary wave is lost resulting in an almost horizontal transition in the speed–energy curve of figure 2 (note that the energy of the perturbation we imposed – approximately 5% in the example shown – also ends up in the radiated field). Other computations of the instability of moderate amplitude elevation waves of varying amplitudes (with energies between 0.2 and 0.7) yield similar results.

It was found in Calvo *et al.* (2002) that at large amplitudes, beyond a ‘limit point’ in the bifurcation curve, the elevation waves regain spectral stability. This result is confirmed here where a variety of perturbations with 5% of the energy of the initial waves did not show instability on the lower branch of the curve in figure 3(a). In figure 3(b–d), a sample time-dependent computation is shown. Note that some of the perturbation energy has remained in the primary solitary wave and has contributed to the outcome of a wave of slightly larger energy and lower speed than the original.

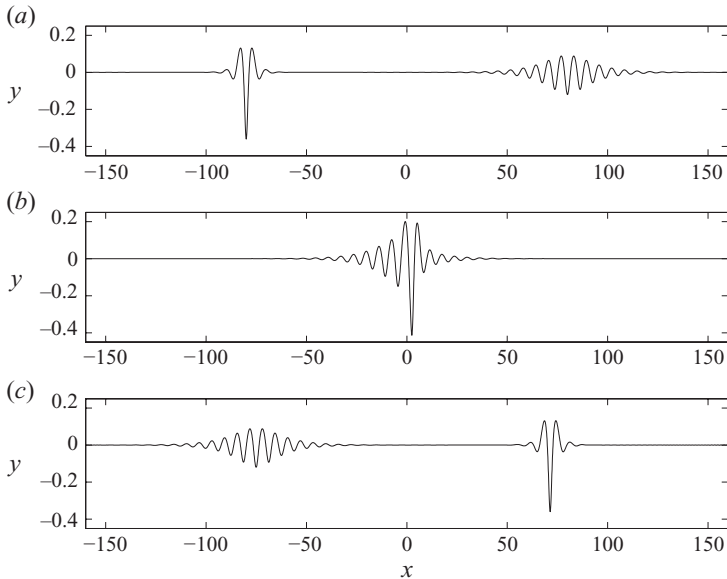


FIGURE 4. Head-on collision of two depression waves of different amplitudes (minimum free-surface heights of -0.36 and -0.12): $t=0$ (a), $t=60$ (b) and $t=110$ (c). The collision is almost elastic with some radiation, invisible to the eye, to the right (ahead) of the larger wave in (c).

We also performed similar stability experiments on depression waves. These were stable in all cases tried.

3.2.2. Collisions

The second set of computational experiments are head-on collisions between stable depression waves, an example of which is shown in figure 4. Several collisions were computed, both symmetric – when both waves are of equal amplitude – and not symmetric, and in all cases the collisions were almost elastic with very little radiation. Close inspection of the computation leading to figure 4 reveals a radiated field of amplitude 10^{-3} . As a measure of robustness of these waves, we also allowed the above computation to continue for long times and despite many head-on collisions due to the periodicity of the domain, the original waves remain essentially unchanged.

The third set of computational experiments are that of overtaking solitary wave collisions: a larger, slower wave is placed ahead of a faster smaller wave. Here we observed two distinct behaviours. An example of the first behaviour is shown in figure 5 whereby the slower wave approaches the larger, and during the collision process it breaks up by transferring some energy to the larger wave and radiating the remaining energy both ahead of the larger solitary wave (in the form of shorter waves) and behind it (in the form of longer waves). Only one wave remains after the collision. This type of collision is observed to happen when the difference in wave amplitudes between the two waves is large.

In figure 6, we present the time evolution of the energy error shown in figure 5, together with the difference between the initial data and the solution obtained numerically by reversing time after $t=3500$ in the collision computation. The surface Euler equations were integrated on a periodic domain $\xi \in [-160, 160)$, with the standard fourth-order Runge–Kutta explicit scheme, with $\Delta t = 0.05$, $N = 4096$ Fourier

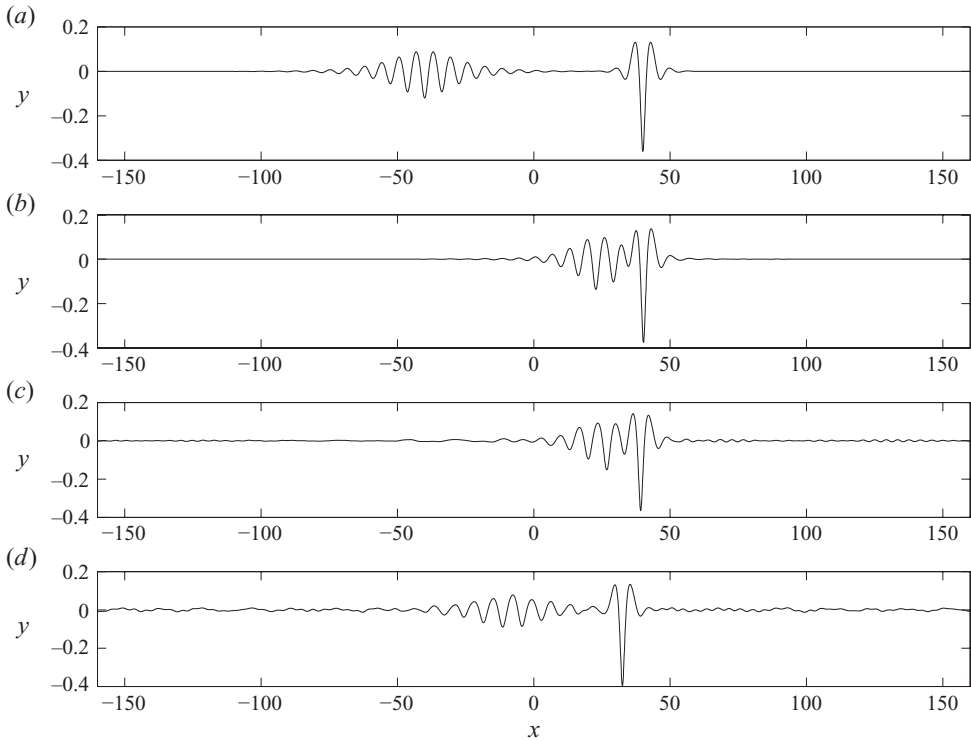


FIGURE 5. Overtaking collision of two depression waves of different amplitudes (minimum free-surface heights of -0.36 and -0.12) shown in a frame of reference moving at the speed of the larger wave. From (a) to (d): $t = 0$, $t = 2000$, $t = 2500$ and $t = 3500$. Only the larger wave survives the collision, with the smaller wavepacket, to the left of it eventually dispersing.

modes, dealiasing with a buffer of N modes (since the nonlinearities are not algebraic, the dealiasing is approximate), and no filtering. We note that the energy of the waves decreased monotonically, and that most of the final time-reversed error is due to a very small phase shift in the initial solitary waves, of the order of 10^{-7} of a carrier wavelength after a nonlinear evolution of order 10^3 carrier wavelengths.

The second type of behaviour occurs when both waves survive the collision, as in figure 7. The collision is also inelastic: the larger wave always gains some energy, the smaller one loses some and there is some radiated wave field. In the process of colliding the waves exchange ‘identities’: the smaller trailing wave grows in amplitude and the larger, leading wave loses amplitude to become the new pair of solitary waves. This results in a backward phase shift for the larger wave and a forward shift for the smaller wave. This type of collision occurs when both waves are of larger amplitude and their amplitude difference is small.

Some collisions of depression waves with the much larger amplitude elevation waves of figure 3 were also computed and show similar behaviour to figure 5: the much larger elevation wave survives, and the depression wave is destroyed in the collision.

For all collision experiments, the initial data were constructed by computing first the two solitary travelling waves individually, by the spectral method described before, but on a large domain. The two waves are then shifted so as to minimize their overlap,

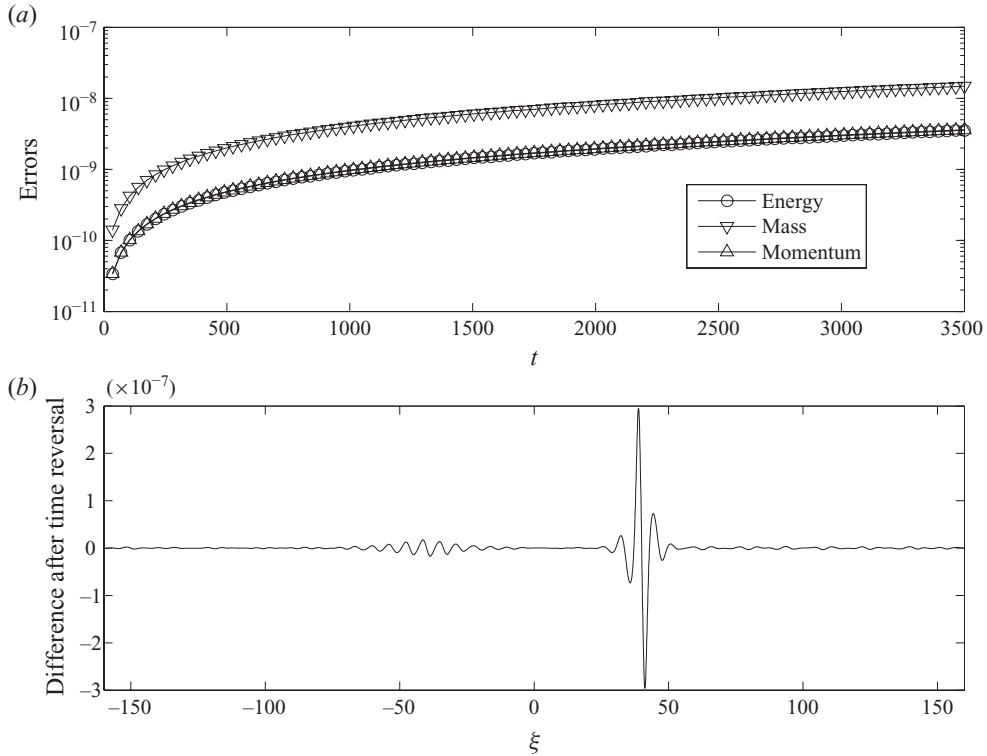


FIGURE 6. Evolution of the errors for the computation shown in figure 5. (a) Relative mass, momentum and energy errors as a function of time. (b) The difference between the initial data and the time reversed solution computed from $t = 3500$ back to $t = 0$.

and the two solutions are added. The accuracy of this superposition method was verified numerically in the case of two equal waves travelling in the same direction – which were seen to travel as a well-separated pair of waves – and was found not to introduce measurable errors (compared to the aforementioned 10^{-8} accuracy of the scheme).

4. Conclusion

An accurate and efficient numerical procedure to compute time-dependent nonlinear gravity–capillary free-surface flows was implemented. The method was used to study the time evolution of wavepacket solitary waves with decaying oscillatory tails. It was found that elevation solitary waves are unstable and evolve into depression solitary waves. On the other hand depression solitary waves of moderate amplitude and certain large amplitude elevation waves were found to be stable in agreement with previous stability analysis. Head-on and overtaking collisions of depression solitary waves were also studied. Collisions are inelastic and some collisions will destroy one of the waves. The nonlinear Schrödinger equation, which is the standard model for wavepacket dynamics, does not predict any of the stability or inelastic collision behaviour that we observed. It only predicts the existence of solitary waves. The behaviour of these waves, however, is qualitatively similar to the models studied by Malomed & Vanden-Broeck (1996) and Akers & Milewski (2008).

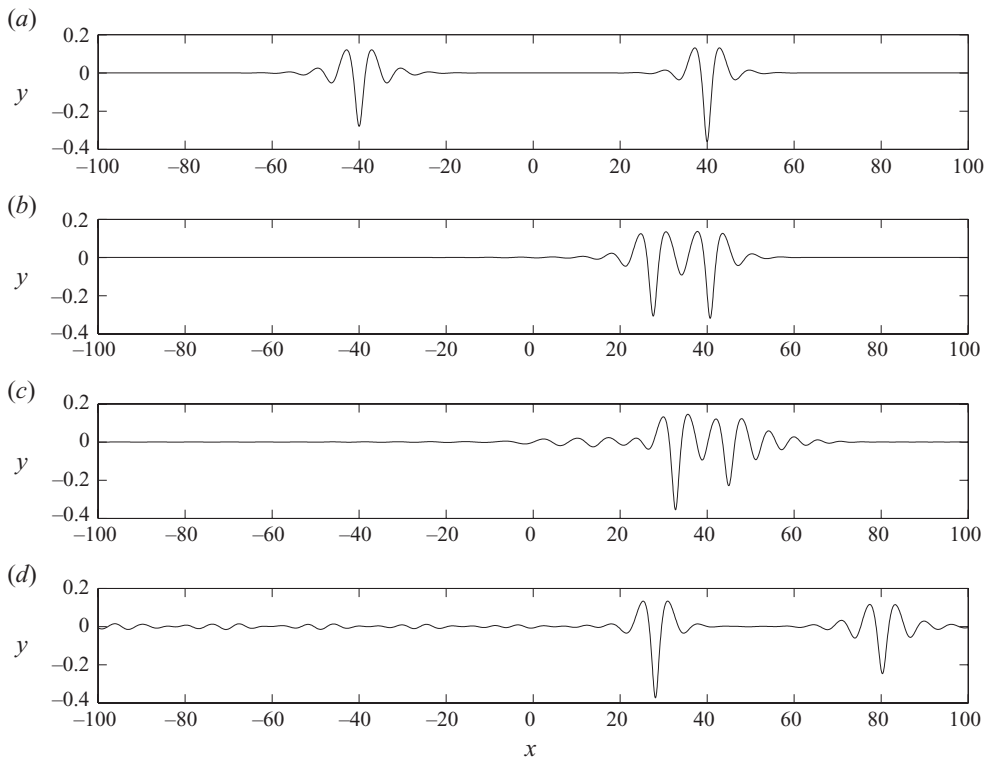


FIGURE 7. Overtaking collision of two depression waves of different amplitudes (minimum free-surface heights of -0.36 and -0.28) shown in a frame of reference moving at the speed of the larger wave. From (a) to (d): $t = 0$, $t = 4000$, $t = 4500$ and $t = 6000$. Both solitary waves survive the collision. Only part of the computational domain is shown.

This work was supported by EPSRC under Grant GR/S47786/01, and by the Division of Mathematical Sciences at the National Science Foundation under Grant DMS 0908077.

REFERENCES

- AKERS, B. & MILEWSKI, P. A. 2008 Model equations for gravity-capillary waves in deep water. *Stud. Appl. Maths* **121**, 49–69.
- AKERS, B. & MILEWSKI, P. A. 2009 A model equation for wavepacket solitary waves arising from capillary-gravity flows. *Stud. Appl. Maths* **122**, 249–274.
- AKERS, B. & MILEWSKI, P. A. 2010 Dynamics of three dimensional gravity-capillary solitary waves in deep water. *SIAM J. Appl. Maths* **70**, 2390–2408.
- BERGER, K. & MILEWSKI, P. A. 2000 The generation and evolution of lump solitary waves in surface-tension-dominated flows. *SIAM J. Appl. Maths* **61**, 731–750.
- CALVO, D. C., YANG, T. S. & AKYLAS, T. R. 2002 Stability of steep gravity-capillary waves in deep water. *J. Fluid Mech.* **452**, 123–143.
- DIAS, F. & IOOSS, G. 1993 Capillary-gravity solitary waves with damped oscillations. *Physica D* **65**, 399–423.
- DIAS, F., MENASCE, D. & VANDEN-BROECK, J.-M. 1996 Numerical study of capillary-gravity solitary waves. *Eur. J. Mech. B: Fluids* **15**, 17–36.
- DIORIO, J., CHO, Y., DUNCAN, J. H. & AKYLAS, T. R. 2009 Gravity-capillary lumps generated by a moving pressure source. *Phys. Rev. Lett.* **103**, 214502.

- DYACHENKO, A. L., ZAKHAROV, V. E. & KUZNETSOV, E. A. 1996 Nonlinear dynamics on the free surface of an ideal fluid. *Plasma Phys. Rep.* **22**, 916–928.
- FALCON, E., LAROCHE, C. & FAUVE, S. 2002 Observation of depression solitary surface waves on a thin fluid layer. *Phys. Rev. Lett.* **89**, 204501.
- GRIMSHAW, R., MALEEWONG, M. & ASANAVANT, J. 2009 Stability of gravity-capillary waves generated by a moving pressure disturbance in water of finite depth. *Phys. Fluids* **21**, 082101.
- GROVES, M. D. & WAHLÉN, E. 2010 On the existence and conditional energetic stability of solitary water waves with weak surface tension. *C. R. Acad. Sci. Paris I* **348**, 397–402.
- IOOSS, G. & KIRRMANN, P. 1996 Capillary gravity waves on the free surface of an inviscid fluid of infinite depth: existence of solitary waves. *Arch. Rat. Mech. Anal.* **136**, 1–19.
- KADOMTSEV, B. B. & PETVIASHVILI, V. I. 1970 On the stability of solitary waves in weakly dispersing media. *Sov. Phys. Dokl.* **15**, 539541.
- KIM, B. & AKYLAS, T. R. 2007 Transverse instability of gravity-capillary solitary waves. *J. Engng Maths* **58**, 167175.
- LI, Y. A., HYMAN, R. J. M. & CHOI, W. 2004 A numerical study of the exact evolution equations for surface waves in water of finite depth. *Stud. Appl. Maths* **113**, 303–324.
- LONGUET-HIGGINS, M. S. 1989 Capillary-gravity waves of solitary type on deep water. *J. Fluid Mech.* **200**, 451–478.
- MALOMED, B. & VANDEN-BROECK, J.-M. 1996 Solitary wave interactions for the fifth-order KdV equation. *Math. Probl. Theory Water Waves, Contemp. Maths* **200**, 133–143.
- PARAU, E. I., VANDEN-BROECK, J.-M. & COOKER, M. J. 2005 Nonlinear three-dimensional gravity-capillary solitary waves. *J. Fluid Mech.* **536**, 99–105.
- VANDEN-BROECK, J.-M. & DIAS, F. 1992 Gravity-capillary solitary waves in water of infinite depth and related free-surface flows. *J. Fluid Mech.* **240**, 549–557.
- ZHANG, X. 1995 Capillary-gravity and capillary waves generated in a wind wave tank: observations and theory. *J. Fluid Mech.* **289**, 51–82.